Geng *et al.*
Chinese Journal of Mechanical Engineering (2022) 35:139
https://doi.org/10.1186/s10033-022-00808-y

Chinese Journal of Mechanical Engineering

ORIGINAL ARTICLE

Open Access

Fabrication of Ordered Micro/Nanostructures Using Probe-Based Force-Controlled Micromachining System

Yanquan Geng[1,2], Yuzhang Wang[1,2], Jianxiong Cai[2], Jingran Zhang[3] and Yongda Yan[1,2*]

Abstract

This paper presents a probe-based force-controlled nanoindentation method to fabricate ordered micro/nanostructures. Both the experimental and finite element simulation approaches are employed to investigate the influence of the interval between the adjacent indentations and the rotation angle of the probe on the formed micro/nanostructures. The non-contacting part between indenter and the sample material and the height of the material pile-up are two competing factors to determine the depth relationship between the adjacent indentations. For the one array indentations, nanostructures with good depth consistency and periodicity can be formed after the depth of the indentation becoming stable, and the variation of the rotation angle results in the large difference between the morphology of the formed nanostructures at the bottom of the one array indentation. In addition, for the indentation arrays, the nanostructures with good consistency and periodicity of the shape and depth can be generated with the spacing greater than 1 μm. Finally, Raman tests are also carried out based on the obtained ordered micro/nanostructures with Rhodamine probe molecule. The indentation arrays with a smaller spacing lead to better the enhancement effect of the substrate, which has the potential applications in the fields of biological or chemical molecular detection.

Keywords: Ordered micro/nanostructure, Probe-based micromachining, In-process force-controlled, Indentation array, Micro cutting

1 Introduction

Nowadays, the ordered micro/nanostructure has been widely used in various applications, including preparation for surface enhanced Raman spectra (SERS) substrate [1], superhydrophobic surface [2] and biosensor [3]. How to fabricate the ordered micro/nanostructure in an efficient and low-cost way is an urgent problem to be solved. Up to now, there are many ordered micro/nanostructure technologies, such as photolithography [4], laser processing [5], e-beam lithography [6] and focused ion beam lithography [7]. However, the complex operations, vacuum environment requirement, or expensive equipment and maintenance cost of these mentioned approaches impede their applications. Since its invention, nano-indentation technology has made great progress as a testing technology to measure the properties of materials at the micro and nano scale [8–11], and has been widely used in many fields such as material science, chemistry, and biology. In the process of nanoindentation test, the specimen surface will be deformed when the indenter is pressed into the specimen surface. After the indenter is removed, the specimen surface will be left with indentation caused by the plastic deformation. Therefore, nanoindentation test is not a nondestructive test, and the indentation changes the surface morphology of the specimen. The change of surface morphology can be considered as a fabrication process, thus, the nanoindentation technology can also be regarded as a powerful processing

*Correspondence: yanyongda@hit.edu.cn

[1] Key Laboratory of Micro-systems and Micro-structures Manufacturing of Ministry of Education, Harbin Institute of Technology, Harbin 150001, China
Full list of author information is available at the end of the article

technology to fabricate various micro/nanostructure due to its achievable nanoscale accuracy, ability to operate in an atmospheric environment and the large range of materials to be machined [12–14].

Chang et al. [12] utilized the nanoindentation technology to fabricate nanoindentation arrays on the Au film. A Berkovich diamond indenter is employed to machine inverted triangular pyramid nanopits arrays structures, and the indentation depth and spacing value were used as main parameters to control the morphology of the nanopits arrays. The fabricated nanostructures are then employed as a SERS substrate to detect 2-Nitro-5-thiobenzoic acid (NTB) solution. Yao et al. [14] also used the nanoindentation technology to fabricate nanostructures on the Au thin-film, while, the spacing value chosen for the nanoindentation process was much smaller. Due to the reduced spacing, the superposition between the nanopits was larger, forming more cavities with SERS enhanced effect, which can be used for the SERS detection of low concentration hepatitis virus core antigen. Due to owning the limitations of low efficiency, small range, and small normal load of the commercial nanoindentor, some scholars have developed a variety of set-ups for the processing characteristics of nanoindentation [15–17]. Yan et al. [15] proposed a structured surface fabrication method combining micro-indentation and ultra-precision cutting process. The obtained structured surface can be used to improve the service life and wear resistance of molds in glass or injection molding. Jeon et al. [16] developed a large-scale indentation system with an indentation frequency of 10 Hz and a processing range of 250 mm × 250 mm, which could be used to produce lens arrays with a depth in the range from 1 μm to 6 mm. In our previous study, a probe-based force-controlled nanoindentation system with a four-beam spring was proposed [17]. The orientation of the probe can be controlled by a rotating ring, and 20 × 20 nanoindentation arrays were fabricated with the probe rotation angle of 0° and 45° successfully. However, no previous work focusing on the formation mechanism of the ordered indentation arrays is found up to now.

Therefore, in the present study, both experimental and finite element (FE) simulation approaches are used to study the formation process of the ordered indentation arrays. The machining processes of one array and several arrays indentations are studied. The influences of the internal value and the rotation angle of the probe on the machining outcomes are investigated in details. The surface enhanced Raman scattering (SERS) measurement is also conducted with the machined ordered micro/nanostructures.

2 Methodology

2.1 Experimental Details

In this study, a home-made probe-based force-controlled micromachining system is employed to conduct all the indentation tests. As shown in Figure 1a, the probe is fixed onto a four-beam spring, and the interaction force between the probe and the sample is controlled by monitoring the deformation of the four-beam spring. The rotating ring is used to determine the orientation of the probe, and the locking screw is used to fix the probe. The detail information of this probe-based force-controlled micromachining system can be found in our previous study [17]. A Vickers indenter (Synton-MDP LTD, Switzerland) is selected to carry out the indentation process, and the SEM image of the Vickers indenter used in this study is shown in Figure 1b. As shown in Figure 1c, the included angle between the surface and the axis of the indenter is 68°, and the radius of the indenter is about 200 nm, which is provided by the manufacturer. A pure aluminum block (Hefei Ke Jing Materials Technology Co., Hefei, China) is selected as the sample. The thickness of the pure aluminum block is 1 mm, and the sample surface is polished to achieve the surface roughness (Ra) less than 10 nm. The roughness is measured in the range of 50 μm × 50 μm using tapping mode with a new silicon AFM tip (RTESPA-300, Bruker Company, Germany). Due to the hardness of the diamond material much larger than that of the pure aluminum, the wear of the Vickers indenter can be neglected.

Previous studies have shown that under visible light or near infrared excitation light, the SERS performance of rough aluminum surface is poor, while, rough gold, silver or copper surface has a strong surface enhancement effect [18–20]. Therefore, a gold film was coated on the machined aluminum-based ordered micro/nanostructure to prepare Au-Al surface-enhanced Raman substrate in this study, and the Schematic diagram of Raman detection principle is shown in Figure 2. The interaction of Au surface plasma, measured molecules and laser at the bottom of the machined indentation arrays is easy to generate local electromagnetic field enhancement effect, forming Raman scattering enhancement [21]. The detail

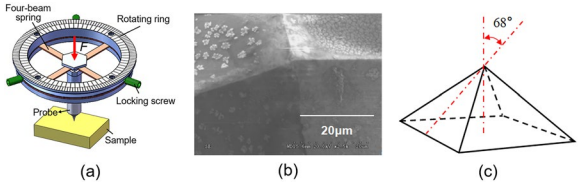

Figure 1 **a** Schematic of a home-made probe-based force-controlled micromachining system, **b** SEM image of the Vickers indenter, **c** geometric schematic of the Vickers indenter

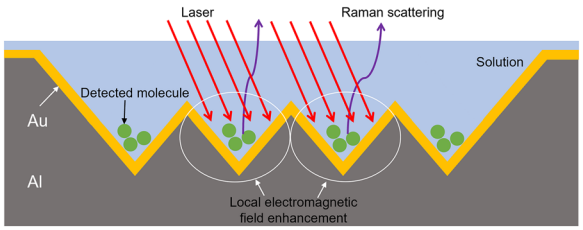

Figure 2 Schematic of Raman detection principle for Au-Al ordered micro/nanostructure substrate obtained based on nanoindentation process

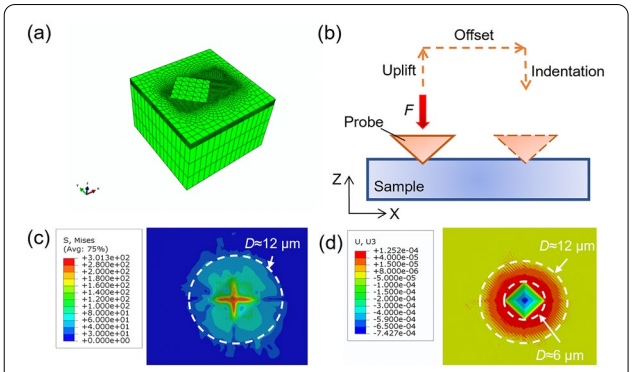

Figure 3 **a** FE model of the nanoindentation, **b** Schematic of the indentation process, **c** Influence region of the residual stress obtained by the nanoindentation with 5 mN, and **d** The corresponding topography of the indentation

procedures for preparing SERS substrate are given as follows. First, ordered micro/nanostructure is machined by indentation process on the pure aluminum block surface. Second, the electron beam deposition approach is utilized to prepare an Au film with a thickness of 20 nm.

2.2 FE Modelling

In the present study, finite element (FE) simulation method was employed to simulate the nanoindentation process with the Vickers indenter by ABAQUS software. Compared with the experimental conditions, the material of the probe was selected as diamond, and the substrate was chosen as a pure aluminum block. The probe was assumed as a rigid body due to the large hardness of the diamond, and the Johnson-Cook constitutive model was used for the material of the aluminum substrate. The detail selection of the parameters of the pure aluminum block substrate for the Johnson-Cook constitutive model was described in our previous work [17]. The probe was set as a rectangular pyramid referring to the geometry of the Vickers indenter, and the substrate is set as a cuboids with dimensional sizes of $30 \times 30 \times 20$ μm^3, as shown in Figure 3a. As shown in Figure 3b, after the first indentation, the probe is lift and is controlled to move an offset value. Then, the probe is pressed into the specimen again to conduct the second indentation. When the normal load is selected as 5 mN, the residual stress and morphology of single-indentation simulated by FEA method are shown in Figures 3c, d, respectively. The diameter of the influence region of the residual stress is about 12 μm, which is observed in Figure 3c. In addition, the depth of the indentation is 742 nm, the diameter of the material pile-up is about 12 μm and the diameter of the subsidence area is about 6 μm, as shown in Figure 3d.

3 Results and Discussion

3.1 Penetrating Structures with Two Patterns

Traditional ultra-precision machining only relies on the relative position relationship between tool and workpiece to realize micro/nanostructure machining [22–24]. The machining accuracy depends on the motion error of each motion axis. In addition, the tool adjusting process before machining is time-consuming. For the in-process force-control micro-machining method, the dimensions of the machined structure depend on the normal load applied to the sample. The machining accuracy relies on the control accuracy of the normal load. To improve the machining accuracy, a soft cantilever is needed to control the force applied onto the sample surface [17, 25–29]. Furthermore, the in-process force-control micro-machining method can realize the tool tracking the sample surface during the machining process. Therefore, there is no need to carry out a strict process of leveling-sample and adjusting-tool before processing. Particularly, for machining on inclined surface or micro-ball surface, in-process force-control micro-machining method shows a strong machining capability, and micro-pits and nano-grooves have been fabricated on the micro-ball surface successfully [30, 31].

In our previous study [17], we have mentioned that the rotatable probe is one of the advantages of the developed machining system. In this study, two position status of the probe is selected for the indentation process. The probe position corresponding to the indentation shown in Figure 3 is defined as the initial position, that is, the rotation angle of 0°. Two position status of the probe are selected as indentation with the rotation angles of 0° and 45°. Figure 4 shows the simulation results for the two patterns with a normal load of 5 mN, three different intervals and rotation angles of 0°. According to the diameters of the material pile-up and the subsidence area shown in Figure 3, three typical intervals between the two patterns are chosen as 12 μm, 4 μm and 2 μm, respectively. When the interval is selected as 12 μm, the ranges of the material pile-ups for the two patterns are just tangential without superposition, and both the depths of the two

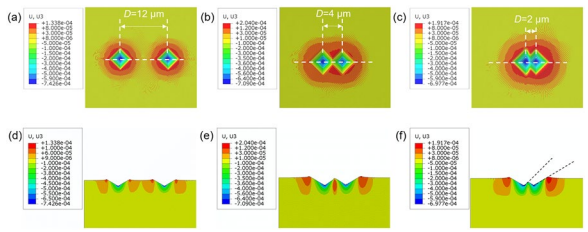

Figure 4 Top views of the simulated results for the two adjacent indentations with the rotation angle of 0° and the spacings of **a** 12 μm, **b** 4 μm and **c** 2 μm; Side views of the simulated results for the two adjacent indentations with the rotation angle of 0° and the spacings of **d** 12 μm, **e** 4 μm and **f** 2 μm

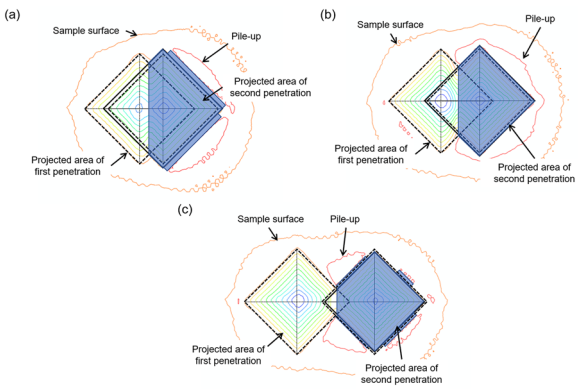

Figure 5 Schematic of projected area of the contact area between the two adjacent indentations with spacings of **a** 1 μm, **b** 2 μm and **c** 4 μm

patterns are 743 nm, which is the same with the case of the single indentation, as shown in Figure 4a, d. It indicates that there is no influence between the two penetrating processes. When the interval is 4 μm, the second indentation is conducted on the material pile-up of the first pattern, as shown in Figure 4b, e. Both the stacking and subsidence areas of the two indentations are overlapped, and the depths of the first and second patterns are 709 nm and 679 nm, respectively, which are smaller than those obtained in the single indentation process. It can be found that the depth of the second pattern is also smaller than that of first pattern, and the height of the material pile-up around the second pattern is larger than that obtained in the single indentation process. When the interval is selected as 2 μm, the second indentation is conducted in the subsidence area of the first pattern, as shown in Figure 4c, f. It can be observed that the stacking and subsidence areas of the two indentations are also overlapped, and the depths of the first and second patterns are 680 nm and 698 nm, respectively. The depth of first pattern is slightly smaller than that of the second pattern. In addition, it can be found from Figure 4f that the slope of right side of the first pattern is reduced due to the material extrusion during the second indentation process.

In order to further investigate the reason of the depth variation of the two patterns after the second penetration with different intervals, three simulations are performed with the intervals of 1 μm, 2 μm and 4 μm, respectively. The normal load and the rotation angle of the indenter are also selected as 5 mN and 0°, respectively. The corresponding projection areas of the two indentations are shown in Figure 5, and the blue areas represent the projection of the contact area between the indenter and the sample materials. The area enclosed by the dotted line is denoted as the projection area of the first penetration. When the interval between the two indentations is less than 6 μm, the subsidence areas of the two indentations will be overlapped, which leads to the left part of the indenter not contacting with the sample material, as shown in Figure 5. This indenter-sample non-contacting area is increased with the interval between the two indentations decreasing. While, the material pile-up is larger around the second pattern as mentioned above, which can partly make up the projected area of the non-contacting part. When the interval is 1 μm, the non-contacting area is relatively larger, and the increase of the indenter-sample contact area caused by the enlarged material pile-up can not fully make up the non-contacting part, as shown in Figure 5a. Thus, the indenter should be pressed into the sample surface deeper to increase the contact area between the indenter and the sample materials for the second indentation. Moreover, in the second penetration process, the materials can be pushed back into the first pattern, which leads to the reduce of the depth of the first pattern. When the interval is enlarged to 2 μm, the non-contacting part between the indenter and the sample material can mainly be balanced by the increase of the contact area caused by the pile-ups, as shown in Figure 5b. Therefore, in this case, the depth of the second pattern is slightly larger than that of the first pattern. For the condition of the interval of 4 μm, as shown in Figure 5c, the non-contacting part is relatively small, and the height of the material pile-up is close to that generated in the case of the interval with 2 μm, which can lead to the depth of the second pattern smaller compared with the first pattern. Based on the analysis above, it indicates that the non-contacting part between indenter and the sample material and the height of the material pile-up are two competing factors, which can determine the depth relationship between the first and second patterns.

When the rotation angle of the indenter is changed to 45°, FE simulations are conducted with the normal force

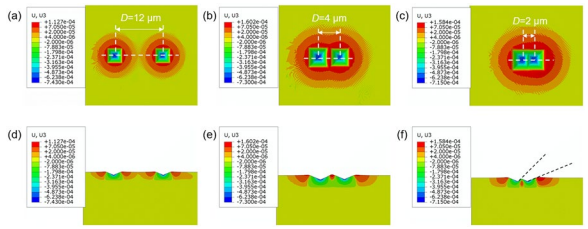

Figure 6 Top views of the simulated results for the two adjacent indentations with the rotation angle of 45° and the spacings of **a** 12 μm, **b** 4 μm and **c** 2 μm; Side views of the simulated results for the two adjacent indentations with the rotation angle of 45° and the spacings of **d** 12 μm, **e** 4 μm and **f** 2 μm

of 5 mN and three intervals of 12 μm, 4 μm and 2 μm. As shown in Figure 6a, when the interval is 12 μm, the ranges of the materials pile-up of the two patterns are also tangential. Thus, the depths of the patterns are the same of 743 nm, as shown in Figure 6d. When the interval is chosen as 4 μm, it can be found from Figure 6b that the subsidence areas of the two patterns are just overlapped, and the second penetration is conducted on the material pile-up of the first pattern. The depths of the first and second patterns are 732 nm and 675 nm, respectively, as shown in Figure 6e. The reduce of the depth of the second pattern results from the increasing of the contact area between the indenter and the material pile-up. The influence of the second penetration on the decreasing of the depth of the first pattern for the case with the rotation angle of 0° is less than that with the rotation angle of 45°. The possible reason is that the overlapped subsidence areas of the two patterns obtained with the rotation angle of 0° is smaller, and less materials are pushed back into the first pattern. When the interval is selected as 2 μm, as shown in Figure 6c, the subsidence areas of the two patterns are overlapped. The depths of the first and second patterns are 682 nm and 715 nm, respectively, as shown in Figure 6f. The depth of the second pattern obtained with the rotation angle of 45° is larger than that penetrated with the rotation angle of 0°. The possible reason is that the projected area of the non-contacting part between the indenter and the sample material for the second indentation in the case of the rotation angle of 45° is larger than that of the rotation angle of 0°, and the indenter needs to penetrate deeper to enlarge the contact area between the indenter and the sample material to balance the applied normal force. In addition, further simulations have been conducted to investigate the relationship between the interval, the depths of the patterns and the height of the materials pile-up. Seven intervals have been selected in the range from 1 μm and 12 μm, and the simulation results are shown in Figure 7. It can be found that the depth of the first penetration is decreased with the interval between the two patterns decreasing for both conditions with the rotation angles of 0° and 45°. While, the depth of the second pattern is decreased first and then goes up with the interval value decreasing. When the interval is larger than 6 μm, the depths of the first and second patterns are close to each other. Moreover, the reducing of the interval value will lead to the increasing of the height of the materials pile-up. It indicates that the pile-ups effect between two indentations occurs when the subsidence areas are overlapped, and the competition between the two factors is the main reason for the depth changing of the second pattern, which are the increase of the probe-sample contact area caused by the enlarged materials pile-up and the non-contacting part resulted from the overlapping.

3.2 Penetration Structures with One Array of Indentations

Further simulations and experiments are conducted to investigate the depth evolution of the patterns during the one array indentations process. First, for the rotation angle of 0°, the normal load is selected as 5 mN, and the intervals are chosen as 1 μm, 2 μm and 3 μm, respectively. Five indentations are carried out from left to right, and the simulation results are shown in Figure 8. Tables 1, 2 and 3 show the changing of the depth for each pattern during the penetration process with different intervals. It can be obtained from these tables that the depth reductions of the first patterns after the second penetration are 114 nm, 62 nm and 35 nm for the intervals of 1 μm, 2 μm and 3 μm, respectively. While, the depth reductions of the first patterns after the third penetration are 14 nm, 9 nm and 1 nm for the intervals of 1 μm, 2 μm and 3 μm, respectively. It indicates that compared with the second penetration, the influence of the third penetration on the depth reduction of the first pattern is less, and the greater the indentation spacing, the smaller the impact. In addition, when the interval is 1 μm, it can be found from Test 5 in Table 1 that the depth of the first pattern is smaller than that of the second pattern, the depths of the second, third and fourth indentations decrease in

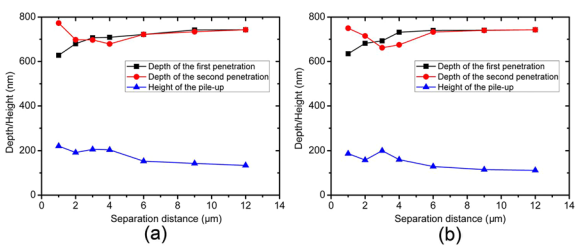

Figure 7 Indentation depth and pile-up height of the two adjacent indentations with the rotation angles of **a** 0° and **b** 45°

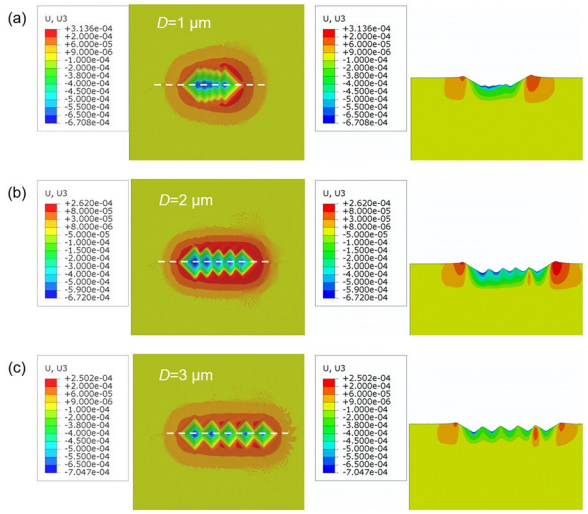

Figure 8 Top views and the corresponding cross-sections of the simulated results for the one array indentations with the rotation angle of 0° and the spacing of **a** 1 μm, **b** 2 μm and **c** 3 μm

Table 1 Depth variation of each indentation during the one array indentations with the rotation angle of 0° and the spacing of 1 μm

Test	First (nm)	Second (nm)	Third (nm)	Fourth (nm)	Fifth (nm)
1	742	–	–	–	–
2	628	773	–	–	–
3	614	687	697	–	–
4	614	672	598	632	–
5	614	671	596	556	642

Table 2 Depth variation of each indentation during the one array indentations with the rotation angle of 0° and the spacing of 2 μm

Test	First (nm)	Second (nm)	Third (nm)	Fourth (nm)	Fifth (nm)
1	742	–	–	–	–
2	680	698	–	–	–
3	671	639	591	–	–
4	670	634	542	616	–
5	670	634	542	542	601

turn, and the depth of the fifth pattern is the largest. When the intervals are selected as 2 μm and 3 μm, as shown in Test 5 in Tables 2 and 3, the depths of the first three patterns decrease in turn, and the depths of the third and the fourth patterns are almost the same. If the processing continues, the depth of the fifth pattern may also be reduced to the depth of the third and fourth patterns due to the subsequent indentation. Therefore, for one array indentations, the depth of the pattern is almost stable after processing three indentations. In addition, the first and last indentations are at the edge positions of the whole process, which are only influenced by the following and previous indentations, respectively. Thus, the depth variation trend of the middle indentation is more representative.

Table 3 Depth variation of each indentation during the one array indentations with the rotation angle of 0° and the spacing of 3 μm

Test	First (nm)	Second (nm)	Third (nm)	Fourth (nm)	Fifth (nm)
1	742	–	–	–	–
2	707	697	–	–	–
3	706	659	634	–	–
4	706	654	580	642	–
5	705	651	580	582	626

The peak-to-trough values of the structures in the middle cross-sections of the patterns are also measured based on the simulation results. Because of the specificity of the first and last indentations, the first and last patterns are not considered. When the interval is 3 μm, the peak-to-trough values of the second, third and fourth structures are 420 nm, 430 nm and 431 nm, respectively. For the case of the interval of 2 μm, the peak-to-trough values of the second, third and fourth structures are reduced to 255 nm, 277 nm and 278 nm, respectively. Moreover, the peak-to-trough values of the second, third and fourth structures are 79 nm, 69 nm and 76 nm, respectively, when conducting indentations with the interval of 1 μm. It can be obtained that the peak-to-trough values of the middle structures are almost the same. In addition, the peak-to-trough values of the middle structures go up with the increasing of the interval between the adjacent patterns, which is contrary to the variation tendency of the machined depth of the patterns. This results from the variation of the overlapping region for different intervals.

For the case of the rotation angle of 45°, the normal force is also chosen as 5 mN, and the intervals are selected as 1 μm, 2 μm, and 3 μm, respectively. The simulation results are shown in Figure 9. When the interval is selected as 3 μm, the peak-to-trough values of the second, third and fourth structures are 669 nm, 673 nm and 687 nm, respectively. The peak-to-trough values of the second, third and fourth structures are 472 nm, 472 nm and 460 nm, respectively, when conducting nanoindentation with the interval of 2 μm. While, for the case

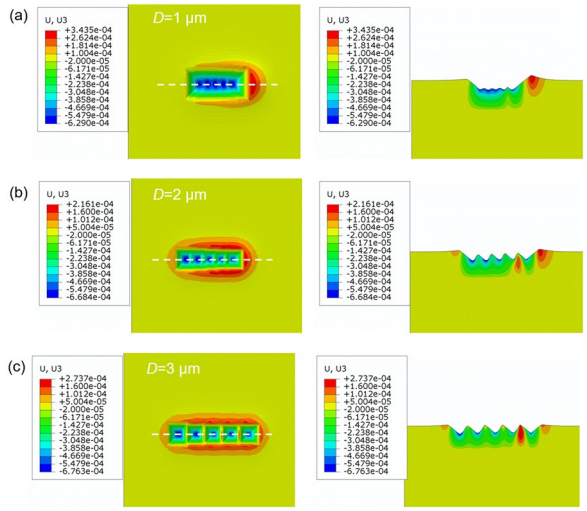

Figure 9 Top views and the corresponding cross-sections of the simulated results for the one array indentations with the rotation angle of 45° and the spacings of **a** 1 μm, **b** 2 μm and **c** 3 μm

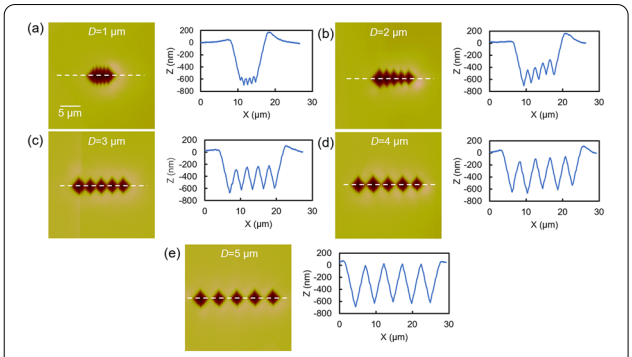

Figure 10 AFM images and the corresponding cross-sections of the experimental results for the one array indentations with the rotation angle of 0° and the spacings of **a** 1 μm, **b** 2 μm, **c** 3 μm, **d** 4 μm and **e** 5 μm

of the interval of 1 μm, the peak-to-trough values of the second, third and fourth structures decrease to 104 nm, 70 nm and 113 nm, respectively. It can be observed that the peak-to-trough values of the middle cross-sections of the patterns obtained with the rotation angle of 45° is much larger than those machined with the rotation angle of 0°. The possible reason is the overlapped subsidence areas of the patterns obtained with the rotation angle of 0° are smaller, and the right contour of the previous pattern removed by the subsequent indentation is less for the case of the rotation angle of 45°.

Figure 10 shows the AFM images and the corresponding cross-sections of the fabricated nanoindentation arrays using Vickers indenter. The normal load is set as 5 mN, the rotation angle is chosen as 0°, and the interval between the adjacent indentations is selected in the range from 1 μm to 5 μm. Five indentation processes for each array are conducted. When the interval is 1 μm, the depth of the second indentation is larger than that obtained by the first indentation, and the depths of the following four indentations decrease in turn. In this case, due to the superposition and extrusion between the adjacent indentations, the subsidence area of the indentations deforms greatly. When the interval is selected as 2 μm, the depths of the first four indentations decrease in turn, and the depth of the last indentation is close to that of the fourth indentation. When the interval value is enlarged to 3 μm, the depths of the first three indentations decrease in turn, and the depth of the last two indentations are close to that of the third indentation. Thus, it can be found that the indentation depth tended to be stable starting from the fourth and third indentation, respectively, with the interval values of 2 μm and 3 μm. Moreover, it can be seen from Figures 10d and e that the indentation depth is almost stable when the spacing values are chosen as 4 μm and 5 μm. It can also be observed from Figure 10 that there are nanostructures on the middle cross-sections of the patterns, similar to the simulation results, and the peak-to-trough values of the obtained nanostructures are about 100 nm, 200 nm, 350 nm, 450 nm and 600 nm for different interval values, respectively. In addition, an obvious accumulation is formed at the end of the indentation column, and the smaller the interval, the higher the accumulation.

Figure 11 shows the AFM images and the corresponding cross-sections of the fabricated nanoindentation arrays using the Vickers indenter with the rotation angle of 45°. The normal load is also selected as 5 mN, and the internal values in the range from 1 μm to 5 μm are used in the indentation process. When the internals are chosen as 1 μm and 2 μm, the indentation depth increases

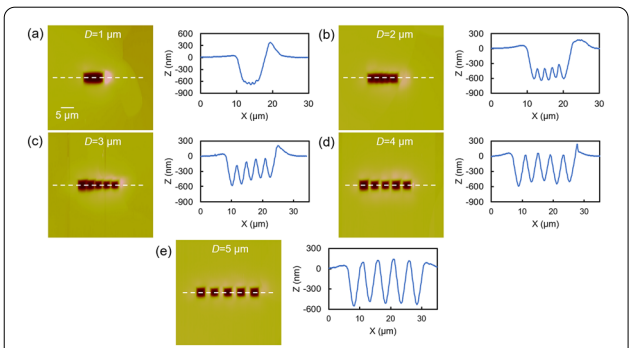

Figure 11 AFM images and the corresponding cross-sections of the experimental results for the one array indentations with the rotation angle of 45° and the spacings of **a** 1 μm, **b** 2 μm, **c** 3 μm, **d** 4 μm and **e** 5 μm

first and then decreases. When indenting with the internal of 3 μm, the indentation depth gradually decreases. When the internal value is enlarged to 4 μm, the indentation depth decreases first and then tends to be stable. When the internal value reaching to 5 μm, the indentation depth changes little, basically stable. In the case of the internal value of 1 μm, the deformation of the micro pits at the bottom of the indentation array is serious, and the depth consistency is poor. When the internal values are selected as 2 μm, 3 μm, 4 μm and 5μm, nanostructures with good consistency of shape and depth are formed at the bottom of the indentations array, and the peak-to-trough values of the nanostructures are 220 nm, 400 nm, 530 nm and 600 nm, respectively. At the end of the indentation array, a more obvious accumulation is also formed, and the smaller the spacing, the higher the accumulation.

Compared with the FE simulation results, the overall trend of the indentation depth is similar. The larger the spacing, the more similar the shape of the micropits formed in the indentation process to the shape of the probe, the better the shape, depth consistency and periodicity are. Moreover, the single row of indentation morphology shows a great difference when conducting indentation with different rotation angles of the probe. However, the peak-to-trough values of the nanostructures obtained by the experimental tests are smaller than those obtained by simulation method. The possible reason can be given as follows. The indenter used in the experimental tests has a radius of about 200 nm, while, in the simulation model, the indenter is assumed as a triangular pyramid without considering the tip radius. Thus, the depth of the nanostructures obtained by experimental tests are smaller than those of simulation results. Meanwhile, due to the larger non-contacting part between the indenter and the sample material for the case of rotation angle of 45°, the influence of the assumption of the probe for the simulation is greater. Therefore, the difference between the experimental and simulation resulted is larger when indenting with rotation angle of 45°.

As shown in Figure 12, the Vickers indenter with the normal load of 5 mN and the rotation angle of 0° is employed to proceed long-array indentations with different internal values. The internal values are selected as 1 μm, 2 μm, and 3 μm, and the indentation numbers are 60, 30 and 20 for each internal value. The process order is from top to bottom. When the internal value is selected as 1 μm, the second indentation is deeper than the first indentation, the second to the tenth indentation depths gradually decrease, and the depths of the subsequent indentations are basically stable at about 350 nm, forming periodic nanostructure with a peak-to-trough

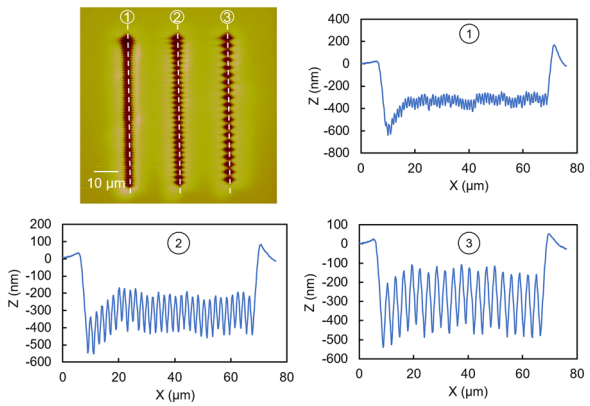

Figure 12 **a** AFM image and the corresponding cross-sections of the experimental results for the one array indentations with the rotation angle of 0° and the spacings of **b** 1 μm, **c** 2 μm and **d** 3 μm

value of about 100 nm. When the internal value is chosen as 2 μm, the depths of the first six indentations gradually decrease, and the depths of the later indentations are basically stable at about 400 nm, forming a periodic nanostructure with a peak-to-trough value of about 200 nm. In the case of the internal value of 3 μm, the depths of the first four indentations gradually decrease, and the depth of the later indentation was basically stable at about 450 nm, forming a periodic nanostructure with a peak-to-trough value of about 350 nm. Therefore, it indicates that nanostructures with good depth consistency and periodicity can be formed after the depth of the indentation becoming stable, and the period of the nanostructure is the same with the internal value between the adjacent indentations.

When the rotation angle of probe is selected as 45° and other parameters remain unchanged. The AFM images and the corresponding cross-sections are shown in Figure 13. Compared with the results obtained with the rotation angle of 0°, the variation trend of indentation depth is similar, while, the morphologies of the formed nanostructures at the bottom the indentation arrays show great difference. Moreover, when the internal between the adjacent indentations is chosen as the same value, more indentation is needed to achieve stability for the machining process with the rotation angle of 45°. When the internal values are selected as 1 μm, 2 μm and 3 μm, the peak-to-trough values of the machined nanostructures are 20 nm, 150 nm and 370 nm, respectively. The reason for the difference between the experimental and simulation results is mentioned above, that is, the assumption of the indenter without considering the radius of probe apex is the main factor. In addition, the period of the nanostructure is also the same with the

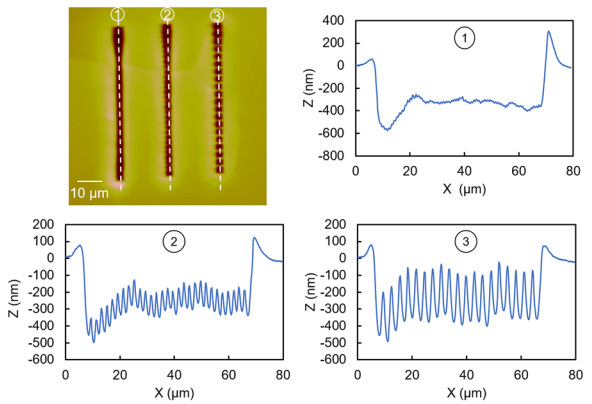

Figure 13 **a** AFM image and the corresponding cross-sections of the experimental results for the one array indentations with the rotation angle of 45° and the spacings of **b** 1 μm, **c** 2 μm and **d** 3 μm

spacing value between the adjacent indentations in this case.

3.3 Penetration Structures with Arrays of Indentations

The process of the arrays of indentations to fabricate two-dimensional penetration structures is also investigated by experimental and simulation approaches in this study. In the machining process of the indentation arrays, the indentation in the middle of the array is affected by all the adjacent indentations around it. Thus, 3 × 3 arrays of indentations are simulated by FE method by Vickers indenter, and the central indentation can be affected by the surrounding eight indentations. Figure 14 shows the machining procedure of the arrays of indentations, which is processed in columns. Figure 15 shows the simulation results of 3 × 3 arrays of indentations conducted with the normal load of 5 mN, the rotation angle of 0° and different internal values. When the spacing is selected as 1 μm, the superposition area of the indentations is large, the serious deformation can be formed in the subsidence area, and the shape quality and depth consistency of the nanostructure formed at the bottom of the indentation arrays is poor. When the internal values are chosen as 2 μm and 3 μm, the indentation overlapping area is smaller, and the shape quality and depth consistency of the nanostructure formed at the bottom of the indentation arrays is better. The accumulation height increases with the indentation processing, and the accumulation on the right side of the indentation arrays is the most obvious.

Figure 16 shows the change of the deformation for the fifth indentation center point of the indentation arrays in Z direction with the time. The upward direction is defined as the positive direction of coordinate axis in Figure 16. When the internal value is chosen as 1 μm, the first, second, and fourth indentations all deform the

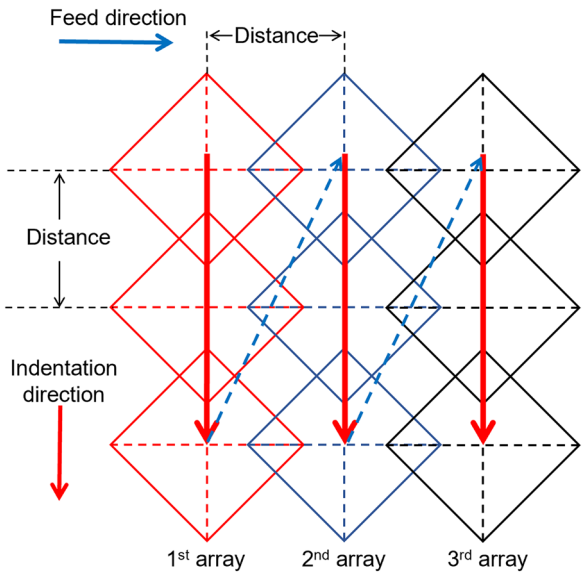

Figure 14 Schematic of machining procedure of the arrays of indentations

center point of the fifth indentation downward, as shown in Figure 16a, because the center point of the fifth indentation is in their subsidence area. After finishing the first four indentations, the fifth indentation center point was deformed by − 450 nm. The actual pressing depth of the fifth indentation is about 370 nm. When processing the sixth indentation, the deformation of the center point of the fifth indentation shows upward, and the indentation

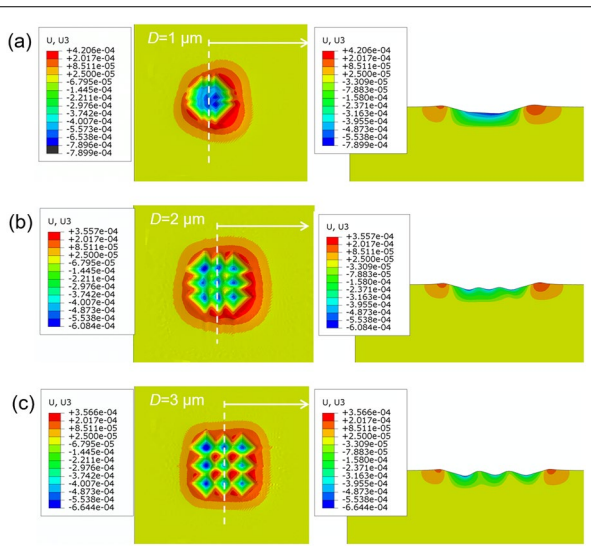

Figure 15 Top views and the corresponding cross-sections of the simulated results for the 3 × 3 indentation arrays with the rotation angle of 0° and the spacings of **a** 1 μm, **b** 2 μm and **c** 3 μm

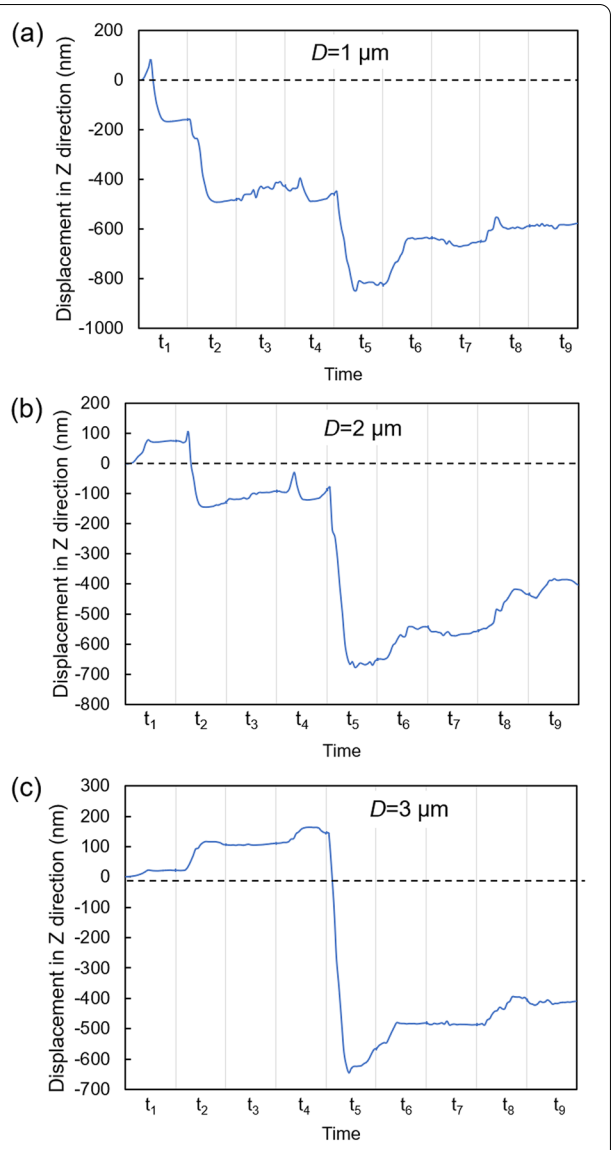

Figure 16 Change of the deformation for the fifth indentation center point of the 3 × 3 indentation arrays obtained by the rotation angle of 0° in *Z* direction with the time for the spacings of **a** 1 μm, **b** 2 μm and **c** 3 μm

depth decreases, because the fifth indentation is extruded by the sixth penetration. When the seventh, eighth and ninth indentation is processed, the center point of the fifth indentation produces a small upward deformation, and the indentation depth is further reduced. The final depth of the fifth indentation is 577 nm.

When the internal value between the adjacent indentations is selected as 2 μm, the first indentation deforms the center point of the fifth indentation upwards, and the second indentation deforms the center point of the fifth indentation downwards, as shown in Figure 16b. The

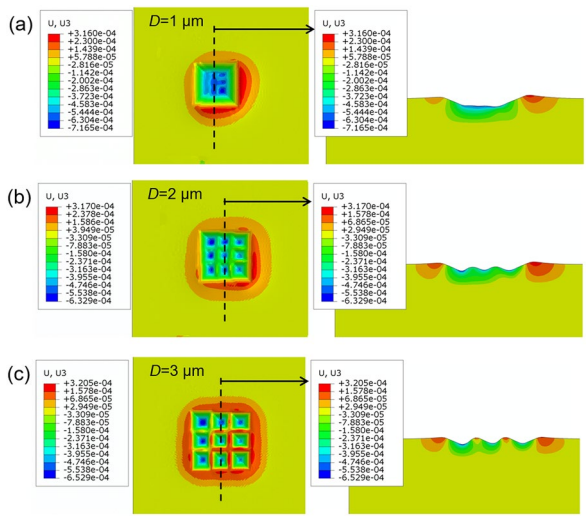

Figure 17 Top views and the corresponding cross-sections of the simulated results for the 3 × 3 indentation arrays with the rotation angle of 45° and the spacings of **a** 1 μm, **b** 2 μm and **c** 3 μm

possible reason can be given as follows. The fifth indentation is farther from the center of the first indentation, located in its accumulation area, and closer to the second indentation, located in its subsidence area. The third indentation has little effect on the center point of the fifth indentation. The fourth indentation deforms the center point of the fifth indentation downward. After finishing the first four indentations, the fifth indentation center point was deformed by − 78 nm, and the actual pressing depth of the fifth indentation at this time is about 570 nm. For the last four indentations, the eighth indentation causes the fifth indentation to produce a small upward deformation at the center point, while, the other three indentations have little influence. The final depth of the fifth indentation is 401 nm.

When the internal value is chosen as 3 μm, as shown in Figure 16c, the first four indentations cause the fifth indentation center to deform upward at 140 nm, and the second indentation has the greatest impact. The actual insertion depth of the fifth indentation is about 700 nm after the first four indentations. The sixth and eighth indentations deform the center of the fifth indentation upward, while, the seventh and ninth indentations have little effect due to large distance to the fifth indentation. The final depth of the fifth indentation is 410 nm.

Figure 17 shows the simulation results of 3 × 3 indentation arrays conducted with the normal load of 5 mN, the rotation angle of 45° and different internal values. At the interval of 1 μm, as shown in Figure 17a, a square pit with a flat bottom is formed, which has a larger depth and width. When the spacing are 2 μm and 3 μm, as shown in

Figures 17b, c, regular inverted quadrilateral nanostructures are formed, with better consistency in shape and depth. With the same internal value, the height of the materials accumulated on the sides of the indentation arrays is less than that obtained by the rotation angle of 0°. Moreover, at the intervals of 1 μm and 2 μm, the material accumulation is concentrated on the right and bottom of the indentation arrays. When the interval value is selected as 3 μm, the accumulation around the indentation array is more average. Thus, the rotation angle has a great influence on the morphology of the indentation arrays.

The variation curve of *z*-direction deformation at the fifth indentation center point of 3 × 3 indentation arrays with time is also extracted for the case of the rotation angle of 45°, as shown in Figure 18. When the spacing is 1 μm, as shown in Figure 18a, the center of the fifth indentation is deformed by − 320 nm after processing the first four indentations. The actual pressing depth of the fifth indentation at this time is about 430 nm. The processing of the last four indentations resulted in the upward deformation of the center point of the fifth indentation, and the indentation depth was further reduced, with the final depth of 551 nm. When the internal value is selected as 2 μm, as shown in Figure 18b, the center point of the fifth indentation was deformed for 145 nm after processing the first four indentations. The actual depth of the fifth indentation is about 718 nm at this time. The last four indentations deform the center of the fifth indentation upwards, and the final depth of the fifth indentation is 420 nm. In the case of the spacing of 3 μm, as shown in Figure 18c, the first four indentations deformed the center of the fifth indentation by 108 nm. The actual depth of the fifth indentation is about 650 nm at this time. The last four indentations deform the center of the fifth indentation upwards, and the final depth of the fifth indentation is 450 nm.

In summary, before the fifth indentation, the position of the indentation center has been deformed, which has an impact on the actual depth of the fifth indentation. As a result of extrusion, the subsequent indentation processing will reduce the depth of the fifth indentation. The final depth of the fifth indentation is different from the single point indentation or single row indentation. Therefore, in the process of indentation arrays, the indentation depth is not only affected by the load and material, but also affected by the adjacent indentations. The internal value and rotation angle are the most important parameters affecting the topography of the indentation arrays, and the internal value plays a key role in the formation of ordered micro/nanostructures. When the spacing was 1 μm, an ordered micro/nanostructure is difficult to be formed at the bottom of the indentation arrays. While, when the spacing increases to 2 μm and 3 μm, an ordered micro/nanostructure can be formed.

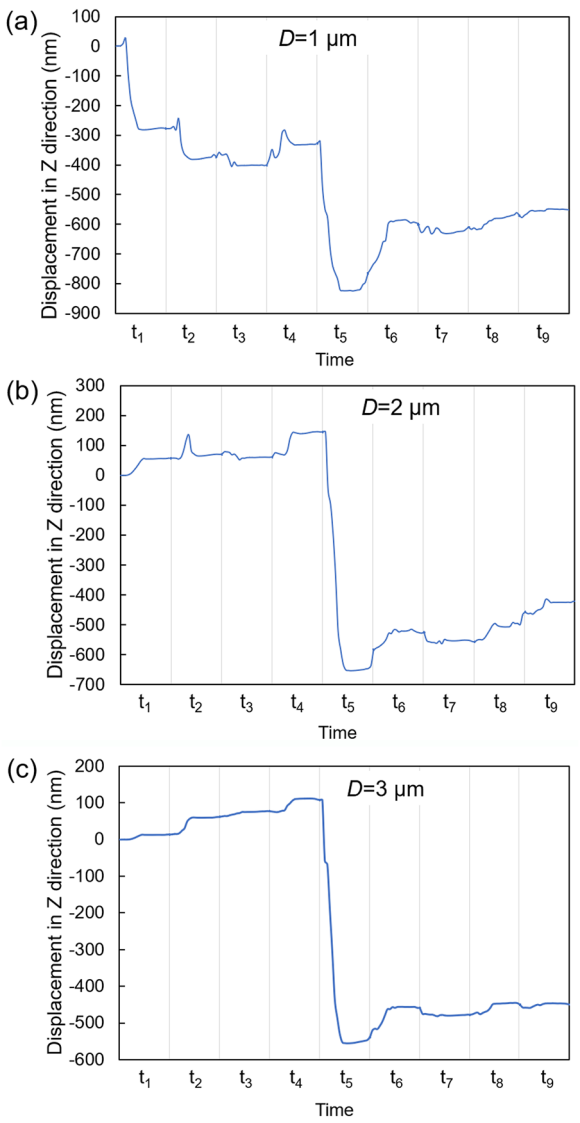

Figure 18 Change of the deformation for the fifth indentation center point of the 3 × 3 indentation arrays obtained by the rotation angle of 45° in *Z* direction with the time for the spacings of **a** 1 μm, **b** 2 μm and **c** 3 μm

In addition to the FE simulation analysis, the experimental 5 × 5 indentation arrays are also performed on the pure aluminum block surface using the Vickers indenter with the rotation angles of 0° and 45°. The normal load is selected as 5 mN, and the internal values are chosen as 1 μm, 2 μm, 3 μm, 4 μm and 5 μm, respectively. The indentation arrays are processed from top to bottom by columns. The AFM images and the corresponding cross-sections of the nanostructures obtained by the

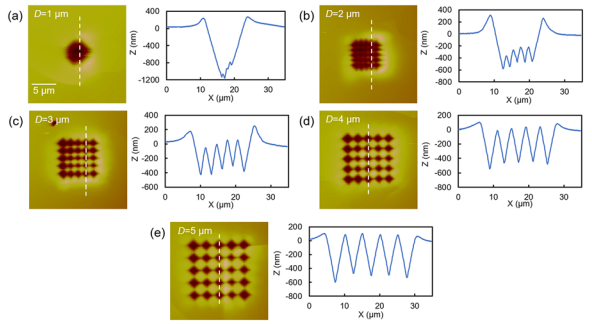

Figure 19 AFM images and the corresponding cross-sections of the experimental results for the 5 × 5 indentation arrays with the rotation angle of 0° and the spacings of **a** 1 μm, **b** 2 μm, **c** 3 μm, **d** 4 μm and **e** 5 μm

rotation angle of 0° are shown in Figure 19. When the internal value is selected as 1 μm, due to the large superposition, the subsidence area is seriously deformed and the inverted quadrilateral pyramid structures are no longer generated. The depth of the indentation arrays in this case can reach to 1.2 μm. When the spacing values are chosen as 2 μm and 3 μm, it can be found from the section of the fourth column that the depths of the first four indentations gradually decrease, and the variation trend of the indentation depths in each column or each row is the same. Thus, the pit with an inclined bottom can be formed by indentation arrays, which is lower in left corner and higher in right corner. In addition, the depth of the last indentation is slightly larger than the previous indentation, indicating that the previous indentations will be extruded by the latter indentation and the depth is reduced, which agrees well with the FE simulation results. In the middle of the indentation array, the inverted quadrilateral pyramid arrays structures with good periodicity are formed. Due to the superposition of the subsidence area, the depths of the formed structures are much smaller than the indentation depths, which are about 200 nm and 350 nm, respectively. When the spacing values are 4 μm and 5 μm, the protruding structures in the middle of the indentation arrays are similar to the quadrigonal table shape, which are separated by micropits. It can be found from the cross-section of the third column that the first indentation is relatively larger and the depths of the latter four indentations are similar. The depths of the formed structures are 500 nm and 650 nm, respectively, and the indentation arrays have good periodicity and consistency of shape and depth. Moreover, the obvious material accumulation can be formed on the lateral of the last row and last column of the indentation arrays.

When the rotation angle is selected as 45°, the grid-shaped structures can be formed in the middle of the indentation arrays, as shown in Figure 20. Compared with the case of the rotation angle of 0°, with the same internal value, the indentation depth obtained with the rotation angle of 45° is smaller, the material accumulation height of the indentation arrays is larger, while, the change rule of the indentation depth is similar. When the spacing is selected as 1 μm, the shape and depth consistency of the structure of the indentation arrays are better than those obtained by the rotation angle of 0°.

In conclusion, for both selected rotation angles, nanostructures with good consistency and periodicity of the shape and depth can be obtained at the bottom of the indentation arrays, when the spacing is greater than 1 μm. The larger the internal value is, the more regular shape of the indentation subsidence area is, the greater the amplitude of the structure is, and the better shape and depth consistency of the structure at the bottom of the indentation arrays. Furthermore, the period of the structure is equal to the spacing between the adjacent indentations.

The 20 × 20 indentation arrays are also conducted by the Vickers indenter with the rotation angles of 0° and 45°. The internal values are selected as 1 μm, 2 μm and 3 μm, respectively. The AFM images and the correspond cross-sections are shown in Figures 21 and 22 for the rotation angles of 0° and 45°, respectively. When the spacing value is chosen as 1 μm, the indentation subsidence area obtained with rotation angles of 0° or 45° is seriously deformed, and the depth of the structure in the middle of the indentation arrays is about 100 nm, which has poor consistency in shape and depth. When the spacing values are selected as 2 μm and 3 μm, most of the indentations are similar in depth, forming structures in the middle of the

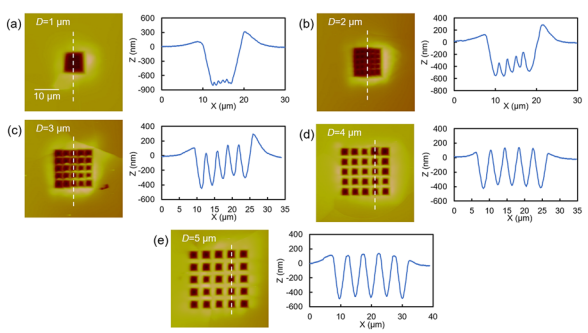

Figure 20 AFM images and the corresponding cross-sections of the experimental results for the 5 × 5 indentation arrays with the rotation angle of 45° and the spacings of **a** 1 μm, **b** 2 μm, **c** 3 μm, **d** 4 μm and **e** 5 μm

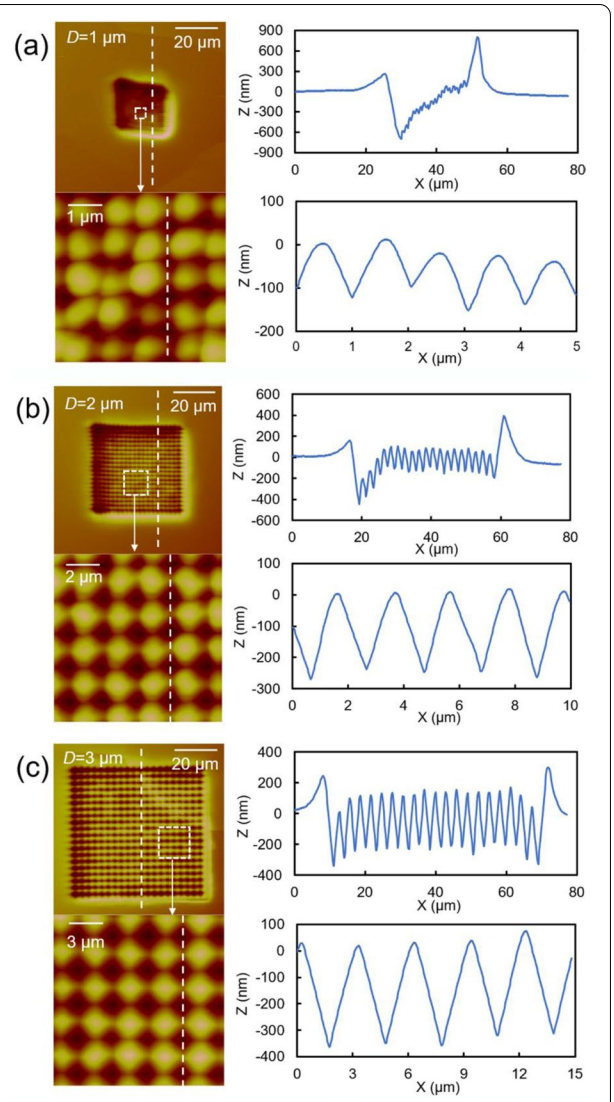

Figure 21 AFM images and the corresponding cross-sections of the experimental results for the 20 × 20 indentation arrays with the rotation angle of 0° and the spacings of **a** 1 μm, **b** 2 μm and **c** 3 μm

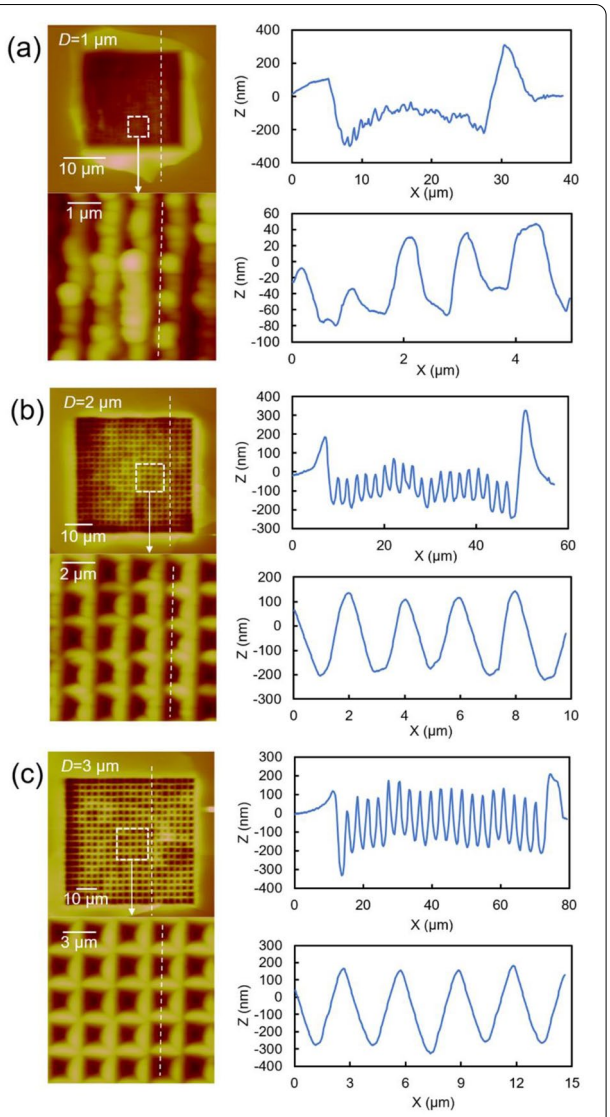

Figure 22 AFM images and the corresponding cross-sections of the experimental results for the 20 × 20 indentation arrays with the rotation angle of 45° and the spacings of **a** 1 μm, **b** 2 μm and **c** 3 μm

indentation arrays with good consistency and periodicity in depth and shape. When the rotation angle of 0°, the depths of the obtained structures are about 250 nm and 350 nm for the spacing of 2 μm and 3 μm, respectively. While, for the case of the rotation angle of 45°, the depths of the structures are 300 nm and 450 nm, respectively. In addition, the period of the structure is equal to the spacing value. At the bottom and right side of the indentation arrays, obvious accumulation is formed. The smaller the spacing is, the higher the accumulation height is.

3.4 SERS Measurement for R6G Using the Machined Structures

In this section, the SERS measurement of the machined structures are conducted, and the SERS substrates are prepared according to the procedure introduced in Section 2.1. Take Vickers indentation arrays with the rotation angle of 0°, the normal load of 5 mN and spacing of 3 μm as an example. The AFM images and corresponding cross-sections of the indentation arrays before and after Au film deposition are shown in Figure 23. It can be found that the morphologies of the indentation arrays before and after Au film deposition

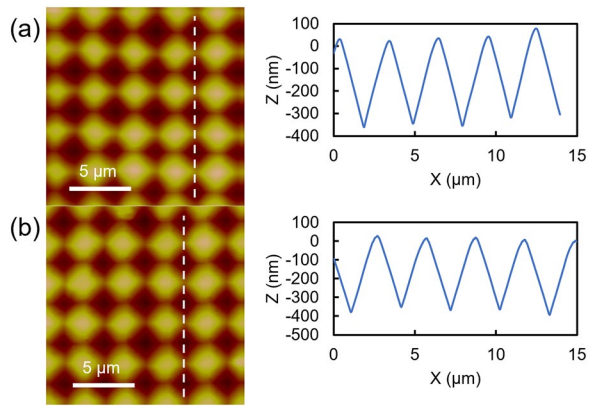

Figure 23 AFM images and the corresponding cross-sections of the nanostructures obtained with the rotation angle of 0° and the spacing of 3 μm (**a**) before and (**b**) after Au film deposition

have almost no change, indicating that the thickness of Au film is very uniform.

A commercial Raman microscopic spectrometer (Renishaw, inVia, UK) is employed to conduct the Raman detection tests. The laser wavelength is 532 nm, the laser power is 1 mW, and the objective lens is 50 times. Rhodamine (R6G) was selected as the probe molecule, which is commonly used to test the SERS performance of the rough surface substrate. The concentration of R6G solution is chosen as 10^{-6} mol/L. The 20 × 20 indentation arrays machined with the rotation angle of 0°, the normal load of 5 mN are selected as the Raman detection substrate. The spacing values are 1 μm, 2 μm and 3 μm, respectively. As shown in Figure 24, the number of spectral peaks of R6G Raman spectrum of Au-Al ordered micro/nanostructure-based indentation arrays with different spacing values is the same, the horizontal axis position of each spectral peak is the same, and the relative height of each spectral peak is also similar. Among them, the wave number of the maximum spectral peak is 1361 cm^{-1}. When the internal values are 2 μm and 3 μm, the peak value of the corresponding Raman spectrum is close to each other. While, the peak value of the corresponding Raman spectra at the spacing value of 1 μm is twice as large as those obtained with the internal values of 2 μm and 3 μm. The smaller the spacing of the indentation arrays is, the higher the peak height of the Raman spectrum is, that is, the better the enhancement effect of the substrate is. Because the smaller the spacing of Vickers indentation array is, the smaller the period and size of the corresponding Au-Al ordered micro/nanostructure are.

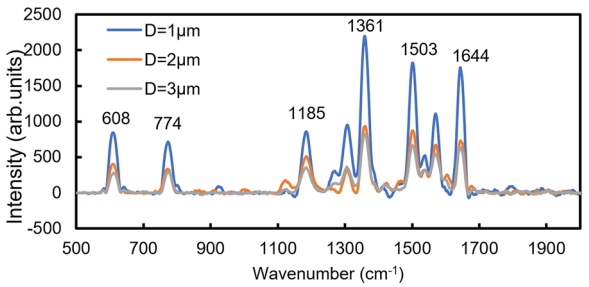

Figure 24 R6G Raman spectra of Au-Al ordered micro/nanostructure substrate obtained by indentation arrays with different spacing values

4 Conclusions

In summary, nanoindentation conducted using a home-made probe-based force-controlled micromachining system is used to fabricate ordered micro/nanostructure on a pure aluminum block. Both experimental and FE simulation approaches are employed to investigate the indentation process. The following conclusions are made:

(1) For the two indentations process, the non-contacting part between indenter and the sample material and the height of the material pile-up are two competing factors, which can determine the depth relationship between the first and second patterns. In addition, the depth of the first penetration is decreased with the interval between the two patterns decreasing, and the depth of the second pattern is decreased first and then goes up with the interval value decreasing.

(2) For the one array indentations, nanostructures with good depth consistency and periodicity can be formed after the depth of the indentation becoming stable. The peak-to-trough values of the middle structures are going up with the increasing of the interval between the adjacent patterns. In addition, the peak-to-trough values of the middle cross-sections of the patterns obtained with the rotation angle of 45° is much larger than those machined with the rotation angle of 0°, and the morphology of the formed nanostructures at the bottom the indentation array shows great difference for different rotation angles.

(3) For the indentation arrays, the internal value plays a key role in the formation of ordered micro/nanostructures. Nanostructures with good consistency and periodicity of the shape and depth can be obtained at the bottom of the indentation arrays, when the spacing is greater than 1 μm. The larger

the internal value is, the better shape and depth consistency of the structure at the bottom of the indentation arrays are.

(4) The Raman tests are also conducted based on the obtained ordered micro/nanostructures with the rotation angle of 0° by the R6G probe molecule. Results show that the smaller the spacing of the indentation arrays is, the better the enhancement effect of the substrate is.

Acknowledgements
Not applicable.

Authors' Contributions
YG: Formal analysis, Data curation, Writing—original draft. YW: Data curation, Writing—original draft. JC: Writing—review and editing. JZ: Writing—review and editing. YY: Formal analysis, Writing—review and editing, Supervision. All authors read and approved the final manuscript.

Authors' Information
Yanquan Geng, born in 1987, is currently a full professor at *Key Laboratory of Micro-systems and Micro-structures Manufacturing of Ministry of Education, Harbin Institute of Technology, China*. He received his doctor degree from *Harbin Institute of Technology, China*, in 2016. His research interests include micro/nanofabrication techniques and the related applications.
Yuzhang Wang, born in 1990, received his doctor degree from *Harbin Institute of Technology, China*, in 2022.
Jianxiong Cai, born in 1993, received his master degree from *Harbin Institute of Technology, China*, in 2018.
Jingran Zhang, born in 1988, currently an associate professor at *Key Laboratory of Cross-scale Micro and Nano Manufacturing, Ministry of Education, Changchun University of Science and Technology, China*. He received his doctor degree from *Harbin Institute of Technology, China*, in 2018.
Yongda Yan, born in 1976, is currently a full professor at *Harbin Institute of Technology, China*. He received his doctor degree from *Harbin Institute of Technology, China*, in 2007.

Funding
Supported by National Natural Science Foundation of China (Grant Nos. 52035004, 51911530206, 51905047), Heilongjiang Provincial Natural Science Foundation of China (Grant No. YQ2020E015), Self-Planned Task of State Key Laboratory of Robotics and System (HIT) (Grant No. SKLRS202001C), and Young Elite Scientist Sponsorship Program by CAST (Grant No. YESS20200155).

Competing Interests
The authors declare no competing financial interests.

Author Details
[1]Key Laboratory of Micro-systems and Micro-structures Manufacturing of Ministry of Education, Harbin Institute of Technology, Harbin 150001, China. [2]Center for Precision Engineering, Harbin Institute of Technology, Harbin 150001, China. [3]College of Mechanical and Electric Engineering, Changchun University of Science and Technology, Changchun 130000, China.

Received: 12 October 2022 Revised: 12 October 2022 Accepted: 21 October 2022
Published online: 21 November 2022

References

[1] X Dou, P Y Chung, H Sha, et al. Large-scale fabrication of nanodimple arrays for surface-enhanced Raman scattering. *Physical Chemistry Chemical Physics*, 2013, 15(30): 12680-12687.
[2] L Feng, S Li, Y Li, et al. Super-hydrophobic surfaces: From natural to artificial. *Advanced Materials*, 2002, 14(24): 1857-1860.
[3] Y S Hsiao, S C Luo, S Hou, et al. 3D bioelectronic interface: Capturing circulating tμmor cells onto conducting polymer-based micro/nanorod arrays with chemical and topographical control. *Small*, 2014, 10(15): 3012-3017.
[4] M Campbell, D N Sharp, M T Harrison, et al. Fabrication of photonic crystals for the visible spectrum by holographic lithography. *Nature*, 2000, 404(6773): 53-56.
[5] J Zhang, J Zhang, A Rosenkranz, et al. Surface textures fabricated by laser surface texturing and diamond cutting-influence of texture depth on friction and wear. *Advanced Engineering Materials*, 2018, 20(4): 1700995.
[6] S Zhu, H H Cheng, I Blakey, et al. Plasmonic 'top-hat' nano-star arrays by electron beam lithography. *Microelectronic Engineering*, 2015, 39: 13-18.
[7] Z W Xu, F Z Fang, Y Q Fu, et al. Fabrication of micro-/nanostructures using focused ion beam implantation and XeF2 gas-assisted etching. *Journal Micromechanics and Microengineering*, 2009, 19(5): 054003.
[8] C Li, X Li, Y Wu, et al. Deformation mechanism and force modelling of the grinding of YAG single crystals. *International Journal of Machine Tools and Manufacture*, 2019, 143: 23-37.
[9] C Li, F Zhang, B Meng, et al. Material removal mechanism and grinding force modelling of ultrasonic vibration assisted grinding for SiC ceramics. *Ceramics International*, 2017, 43: 2981-2993.
[10] H Huang, J W Yan. Investigating shear band interaction in metallic glasses by adjacent nanoindentation. *Materials Science and Engineering: A*, 2017, 704: 375-385.
[11] C Li, Y Wu, X Li, et al. Deformation characteristics and surface generation modelling of crack-free grinding of GGG single crystals. *Journal of Materials Processing Technology*, 2020, 279(5): 116577.
[12] C W Chang, J D Liao, H C Chang, et al. Fabrication of nano-indented cavities on Au for the detection of chemically-adsorbed DTNB molecular probes through SERS effect. *Journal of Colloid and Interface Science*, 2011, 358(2): 384-391.
[13] C Li, F Zhang, X Wang, et al. Repeated nanoscratch and double nanoscratch tests of Lu2O3 transparent ceramics: Material removal and deformation mechanism, and theoretical model of penetration depth. *Journal of the European Ceramic Society*, 2018, 38(2): 705-718.
[14] C K Yao, J D Liao, C W Chang, et al. Spatially reinforced nano-cavity array as the SERS-active substrate for detecting hepatitis virus core antigen at low concentrations. *Sensors and Actuators B: Chemical*, 2012, 174: 478-484.
[15] J Yan, A Horikoshi, T Kuriyagawa, et al. Manufacturing structured surface by combining microindentation and ultraprecision cutting. *CIRP Journal of Manufacturing Science and Technology*, 2012, 5(1): 41-47.
[16] E Jeon, J R Lee, D H Choi, et al. A New application of dynamic indentation: Indentation machining technology. *Experimental Mechanics*, 2017, 57(7): 1127-1133.
[17] Y Geng, J Wang, J Zhang, et al. A probe-based force-controlled nanoindentation system using an axisymmetric four-beam spring. *Precision Engineering*, 2019, 56: 530-536.
[18] Z Q Tian, B Ren, D Y Wu. Surface-enhanced Raman scattering: From noble to transition metals and from rough surfaces to ordered nanostructures. *Journal of Physical Chemistry B*, 2002, 106(37): 9463-9483.
[19] J Wang, Y Yan, S Chang, et al. Label-free surface-enhanced Raman spectroscopy detection of absorption manner of lysozyme based on nanodots arrays. *Applied Surface Science*, 2020, 509: 145332.
[20] J R Zhang, T Q Jia, X Li, et al. Fabrication of nano/microstructures for SERS substrates using an electrochemical method. *Beilstein Journal of Nanotechnology*, 2020, 11: 1568-1576.
[21] J R Zhang, Y D Yan, P Miao, et al. Fabrication of gold-coated PDMS surfaces with arrayed triangular micro/nanopyramids for use as SERS substrates. *Beilstein Journal of Nanotechnology*, 2017, 8: 2271-2282.
[22] C Wang, K Cheng, N Nelson, et al. Cutting force based analysis and correlative observations on the tool wear in diamond turning of single-crystal silicon. *Proceedings of the IMechE, Part B: Journal of Engineering Manufacture*, 2015, 229(10): 1867-1873.
[23] H Liu, W Zong, Z Cui. Durability of micro diamond tools with different crystallographic planes. *Journal of Materials Processing Technology*, 2022, 305: 117600.
[24] H Liu, S Wang, W Zong. Tool rake angle selection in micro-machining of 45 vol.% SiCp/2024Al based on its brittle-plastic properties. *Journal of Manufacturing Processes*, 2019, 37: 556-562.

[25] J Wang, Y Yan, Z Li, et al. Towards understanding the machining mechanism of the atomic force microscopy tip-based nanomilling process, *International Journal of Machine Tools and Manufacture*, 2021, 162: 103701.
[26] Y Yan, J Wang, Y Geng, et al. Material removal mechanism of multi-layer metal-film nanomilling. *CIRP Annals-Manufacturing Technology*, 2022, https://doi.org/10.1016/j.cirp.2022.03.040.
[27] J Wang, Y Yan, B Jia, et al. Study on the processing outcomes of the atomic force microscopy tip-based nanoscratching on GaAs. *Journal of Manufacturing Processes*, 2021, 70: 238-247.
[28] J Deng, J Dong, P Cohen. Development and characterization of ultrasonic vibration assisted nanomachining process for 3D nanofabrication. *IEEE Transactions on Nanotechnology*, 2018, 17(3): 559-566.
[29] H Zhou, C Dmuchowski, C Ke, et al. External-energy-assisted nanomachining with low-stiffness atomic force microscopy probes. *Manufacturing Letters*, 2020, 23: 1-4.
[30] Y Geng, Y Wang, Y Yan, et al. A novel AFM-based 5-axis nanoscale machine tool for fabrication of nanostructures on a micro ball. *Review of Scientific Instruments*, 2017, 88: 115109.
[31] Y Wang, Y Geng, G Li, et al. Study of machining indentations over the entire surface of a target ball using the force modulation approach. *International Journal of Extreme Manufacturing*, 2021, 3: 035102.